Available online at www.sciencedirect.com
ScienceDirect
International Journal of Heat and Mass Transfer 51 (2008) 3840–3853
International Journal of HEAT and MASS TRANSFER
www.elsevier.com/locate/ijhmt

Fundamental consideration of wall heat partition of vertical subcooled boiling flows

G.H. Yeoh [a,*], Sherman C.P. Cheung [b], J.Y. Tu [b], Mark K.M. Ho [a]

[a] Australian Nuclear Science and Technology Organisation (ANSTO), PMB 1, Menai, NSW 2234, Australia
[b] School of Aerospace, Mechanical and Manufacturing Engineering, RMIT University, Victoria 3083, Australia

Received 16 August 2007; received in revised form 15 November 2007
Available online 10 March 2008

Abstract

Improved wall heat flux partitioning accounting sliding bubbles and a mechanistic model that incorporates the fundamental consideration of bubble frequency during low-pressure subcooled flow boiling is presented. A model considering the forces acting on departing bubbles at the heated surface is employed. Coupled with a three-dimensional two-fluid and population balance equations based on the modified MUSIG (MUltiple-SIze-Group) model, the behavior of an upward forced convective subcooled boiling flows in a vertical annular channel is simulated. Comparison of model predictions against local and axial measurements (heat fluxes ranged from 152.9 to 705.0 kW/m^2) is made for the void fraction, Sauter mean bubble diameter and interfacial area concentration covering a range of different mass and heat fluxes and inlet subcoolings. Good agreement is achieved between the predicted and measured profiles. Reasonable agreement with recent experimental measurements is also attained for the predicted growth and waiting times of bubble frequency at particular local wall superheat and subcooling temperatures.

Keywords: Population balance; Bubbly flow; CFD; Average bubble number density

1. Introduction

Modelling subcooled boiling flow especially at low-pressure conditions remains a challenging task. By nature, it is an extremely complex two-phase flow, heat transfer and mass transfer processes. On the heated wall, heterogeneous bubble nucleation occurs within the small pits and cavities which are known as nucleation sites. Subject to external heat, these nucleation sites are activated when its temperature exceeds the liquid saturation temperature of the local pressure. During the nucleation process, the formed vapour bubble grows asymmetrically while it is attached to its nucleation site. With the presence of convective force or buoyancy force and if the boiling flow is vertically orientated, vapour bubble departs from its nucleation site, slides along the heating surface and continues to grow at the downstream until it lifts off from the surface [1]. Fig. 1a illustrates the mechanism of the vapour bubble departing, sliding and lifting off from the heated surface. To aptly model subcooled boiling flows, it is imperative to account the motion of vapour bubbles on the heated surface and its associated thermodynamic non-equilibrium between two phases. It can thus be viewed that calculations carried out without appropriate considerations of these mechanisms can at best only provide a rough estimation of the heat transfer rates from the heated surface as well as the flow characteristics of the whole system.

According to a recent review by Warrier and Dhir [2], a large number of numerical models have been developed to predict the wall heat transfer rates of subcooled boiling flows. These models can be broadly categorised into three approaches: (i) empirical correlations for wall heat flux, (ii) empirical correlations for the partitioning of the wall heat flux, and (iii) mechanistic models for wall heat flux

* Corresponding author. Tel.: +61 2 9717 3817; fax: +61 2 9717 9263.
E-mail address: Guan.Yeoh@ansto.gov.au (G.H. Yeoh).

0017-9310/$ - see front matter © 2008 Elsevier Ltd. All rights reserved.
doi:10.1016/j.ijheatmasstransfer.2007.11.047

Nomenclature

a_{if}	interfacial area concentration (m^{-1})
A_q	fraction of heater area occupied by bubbles
C_1, C_2	constants defined in Eq. (10)
C_D	drag coefficient
C_L	shear lift coefficient
C_p	specific heat ($J\,kg^{-1}\,K^{-1}$)
C_s	constant defined in Eq. (18)
C_v	acceleration coefficient
d	vapor bubble diameter at heated surface (m)
d_w	surface/bubble contact diameter (m)
D	average bubble diameter (m)
D_b	departing bubble diameter (m)
D_d	bubble departure diameter (m)
D_l	bubble lift-off diameter (m)
D_s	Sauter mean bubble diameter (m)
f	bubble frequency (Hz)
f_i	scalar fraction related to the number density of the discrete bubble classes
F	degree of surface cavity flooding
F_b	buoyancy force (N)
F_{cp}	contact pressure force (N)
F_h	force due to the hydrodynamic pressure (N)
F_{du}	unsteady-drag force due to asymmetrical growth of the bubble (N)
F_{qs}	quasi steady-drag force (N)
F_s	surface tension force (N)
F_{sL}	shear lift force (N)
F_x	forces along the x-direction (N)
F_y	forces along the y-direction (N)
F_{lg}	action of interfacial forces from vapor on liquid (N)
F_{gl}	action of interfacial forces from liquid on vapor (N)
F_{lg}^{drag}	drag force (N)
F_{lg}^{lift}	lift force (N)
$F_{lg}^{lubrication}$	wall lubrication force (N)
$F_{lg}^{dispersion}$	turbulent dispersion force (N)
g	gravitational constant ($m\,s^{-2}$)
G	mass flux ($kg\,m^{-2}\,s^{-1}$)
G_s	dimensionless shear rate
h	interfacial heat transfer coefficient
H	enthalpy ($J\,kg^{-1}$)
Ja	Jakob number
k	thermal conductivity ($W\,m^{-2}\,K^{-1}$) or turbulent kinetic energy ($m^2\,s^{-2}$)
K	projected area of bubble (m^2)
h_{fg}	latent heat of vaporization ($J\,kg^{-1}$)
l_s	sliding distance (m)
n_i	number density of the discrete bubble ith class (m^{-3})
N_a	active nucleation site density (m^{-2})
Q_w	wall heat flux ($W\,m^{-2}$)
Q_c	heat transfer due to forced convection ($W\,m^{-2}$)
Q_e	heat transfer due to evaporation ($W\,m^{-2}$)
Q_{tc}	heat transfer (transient conduction) due to stationary bubble ($W\,m^{-2}$)
Q_{tcsl}	heat transfer (transient conduction) due to sliding bubble ($W\,m^{-2}$)
r	bubble radius at heated wall (m) or flow spacing within annular channel (m)
r_c	cavity radius at heated surface (m)
r_r	curvature radius of the bubble at heated surface (m)
Re	bubble Reynolds number
R_f	ratio of the actual number of bubbles lifting off to the number of active nucleation sites
R_i	radius of inner heated wall (m)
R_o	radius of outer unheated wall (m)
s	spacing between nucleation sites (m)
S_i	additional source terms due to coalescence and breakage ($kg\,m^{-3}\,s^{-1}$)
St	Stanton number
t	time (s)
t_g	bubble growth period (s)
t_l	bubble lift-off period (s)
t_{sl}	bubble sliding period (s)
t_w	bubble waiting period (s)
T	temperature (K)
T_b	Bubble internal temperature (K)
T_w	Wall surface temperature (K)
ΔT	difference in temperature (K)
P	pressure ($N\,m^{-2}$)
u	velocity ($m\,s^{-1}$)
u_τ	friction velocity ($m\,s^{-1}$)
v_i	specific volume of discrete bubble ith class ($m^3\,kg^{-1}$)
x	Cartesian coordinate along x
x^+	non-dimensional normal distance from heated wall
y	Cartesian coordinate along y

Greek symbols

α	advancing angle (rad)
α_g	vapor void fraction
α_l	liquid void fraction
β	receding angle (rad)
δ_l	thermal boundary layer thickness (m)
δ_s	surface heater wall thickness (m)
ε	turbulent dissipation rate ($m^2\,s^{-3}$)
η	thermal diffusivity ($m^2\,s^{-1}$)
λ_m^e	effective viscosity (Pa s)
μ	viscosity (Pa s)
θ	bubble contact angle (rad)
θ_i	inclination angle (rad)
ρ	density ($kg\,m^{-3}$)

σ	surface tension (N m^{-1})	inlet	channel entrance
Γ_{lg}	interfacial mass transfer from vapor to liquid (kg m^{-3} s^{-1})	l	liquid
Γ_{gl}	interfacial mass transfer from liquid to vapor (kg m^{-3} s^{-1})	local	local distribution
		s	surface heater
Subscripts		sat	saturation
axial	axial distribution	sub	subcooled
g	vapor	sup	superheated
		w	wall

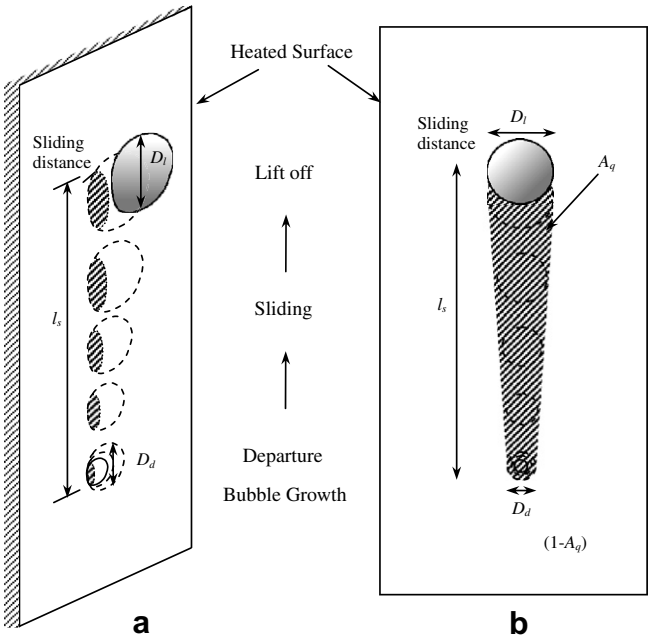

Fig. 1. Schematic drawings illustrating the mechanism of bubble departing, sliding and lifting off from a vertical heated surface forces acting on a growing vapour bubble (a) and the area of influence due to bubble growth and (b) sliding.

and partitioning. It is well known that empirical correlations for wall heat flux are limited to the prediction of total wall heat flux for a particular flow situation. Without modelling considerations on the heat transfer mechanism, this approach provides no information for the partitioning of the wall heat flux making it impossible to determine the vapour generation rate at the wall surface. Nevertheless, empirical correlations for wall heat flux partitioning only provide information on how the wall heat flux is partitioned and cannot be applied to predict the wall heat flux itself.

Mechanistic models have been shown to be able to predict both the wall heat flux and the partitioning of the wall heat flux between the liquid and vapour phases. By employing such an approach, considerations of bubble motions on the heated surface and heat flux partition can be realized by the division of the surface area and heat transfer components into three distinct modes: *single-phase convection*, *transient conduction* and *evaporation*. As demonstrated in Fig. 1b, the transient conduction (quenching of the thermal boundary layer) is assumed to occur over the area of the heater surface under the influence of bubbles (A_q). Conversely, the single-phase convective heat transfer occurs in areas of the heated surface unaffected by the bubbles ($1 - A_q$). The evaporation component which contributes to the vapour generated is related to the volume of the generated bubbles. The mechanistic model developed by Kurul and Podowski [3] is one of the models that have been widely adopted by various researchers [4–6]. It should nonetheless be noted that the Kurul and Podowski model suffers from two major drawbacks.

Firstly, the model is only applicable for subcooled boiling flows where bubbles are immediately released into the bulk subcooled liquid. This assumption may be possibly valid if horizontally orientated pool boiling flow is considered. Nonetheless, as aforementioned, bubbles have shown a tendency to slide before lifting off into the bulk liquid especially in vertical convective subcooled boiling flows. In essence, as indicated in Basu et al. [7,8] and Sateesh et al. [9], the transient conduction due to sliding bubbles in such a case becomes the dominant mode of heat transfer. For vertical subcooled boiling flows, it is therefore important that the wall heat partition model incorporates the area of influence and transient conduction component due to these sliding bubbles.

Secondly, the bubble release frequency, which proportionally affects the quenching heat flux value, is determined by the Cole's empirical correlation [10]:

$$f = \sqrt{\frac{4g(\rho_l - \rho_g)}{3D_b\rho_l}} \tag{1}$$

Although Eq. (1) has been employed rather successfully to solve subcooled boiling flows at high-pressures, the range of applicability of the relationship for low-pressure subcooled boiling flows has however remained debatable. Uncertainty of evaluating the bubble release frequency through empirical correlations should be minimized and replaced by mechanistic approach.

The present study is therefore primarily focused on advancing the existing mechanistic models to incorporate considerations of sliding bubbles and eliminating the uncertainties of applying empirical correlation by

determining the bubble release frequency mechanistically through our earlier development and application of our force balance model [11]. This particular mechanistic model is then incorporated within the framework of two-fluid and our modified MUSIG model [12] to simultaneously handle the bubble coalescence and breakage as well as its condensation processes in the bulk liquid. The numerical model is evaluated through validation against experimental measurements. In this paper, comparisons of model predictions for a range of different mass and heat fluxes and inlet subcoolings are performed against axial measurements of Zeitoun and Shoukri [13] and local measurements of Yun et al. [14] and Lee et al. [15].

2. Mathematical models

2.1. Improved wall heat partition model

Enhancement in heat transfer during forced convective boiling can be attributed by the presence of both sliding and stationary bubbles. There are essentially two mechanisms: (1) the latent heat transfer due to microlayer evaporation and (2) transient conduction as the disrupted thermal boundary layer reforms during the waiting period (i.e. incipience of the next bubble at the same nucleation site).

Transient conduction occurs in regions at the point of inception and in regions being swept by sliding bubbles. For a stationary bubble, the heat flux is given by

$$Q_{tc} = 2\sqrt{\frac{k_l\rho_l C_{pl}}{\pi t_w}}(T_s - T_l)R_f N_a\left(K\frac{\pi D_d^2}{4}\right)t_w f + 2\sqrt{\frac{k_l\rho_l C_{pl}}{\pi t_w}}(T_s - T_l)R_f N_a\left(\frac{\pi D_d^2}{4}\right)(1 - t_w f) \quad (2)$$

where D_d is the bubble departure diameter, T_s is the temperature of the heater surface and T_l is the temperature of the liquid. The first term of the R.H.S. of Eq. (2) accounts for the transient conduction occurred in the projected area of detached bubble during the waiting time. The second term considers the transient conduction happened within the area of growing bubble after the waiting time before bubble departure – the growth period. For a sliding bubble, the heat flux due to transient conduction that takes place during the sliding phase and the area occupied by the sliding bubble at any instant of time is given by

$$Q_{tcsl} = 2\sqrt{\frac{k_l\rho_l C_{pl}}{\pi t_w}}(T_s - T_l)R_f N_a l_s K D t_w f + 2\sqrt{\frac{k_l\rho_l C_{pl}}{\pi t_w}}(T_s - T_l)R_f N_a f t_{sl}\left(\frac{\pi D^2}{4}\right)(1 - t_w f) \quad (3)$$

where the average bubble diameter D is given by $D = (D_d + D_l)/2$ and D_l is the bubble lift-off diameter. Judd and Hwang [16] suggested that the bubble leaving the heater surface draws in liquid from an area called the *area of influence* that is 1.8 times the projected area of the bubble, which is denoted by K. In this study, a value of 1.8 is assumed for K.

The reduction factor R_f appearing in Eqs. (2) and (3) depicts the ratio of the actual number of bubbles lifting off per unit area of the heater surface to the number of active nucleation sites per unit area, *viz.*, $R_f = 1/(l_s/s)$ where l_s is the sliding distance and s is the spacing between nucleation sites. In the present study, it shall be assumed that the nucleation sites are distributed in a square grid and that the bubbles slide only in the direction of the fluid flow [7]. The spacing between nucleation sites can thus be approximated as $s = 1/\sqrt{N_a}$ where N_a, the active nucleation site density, has been obtained from the correlation of Končar et al. [5] expressed as $N_a = [185(T_s - T_{sat})]^{1.805}$. The factor R_f is obtained alongside with the sliding distance evaluated from the force balance model (to be described later). The significance of this factor provides the information whereby the bubble departing from its site of origin merges with other nucleating bubbles at adjacent sites. It is noted that for the case where the sliding distance l_s is less than the spacing s, $R_f = 1$.

Forced convection always prevails at all times in areas of the heater surface that are not influenced by the stationary and sliding bubbles. The fraction of the heater area for stationary and sliding bubbles is given by

$$1 - A_q = 1 - R_f\left[N_a\left(K\frac{\pi D_d^2}{4}\right)t_w f + N_a\left(\frac{\pi D_d^2}{4}\right)(1 - t_w f) + N_a l_s K D t_w f + N_a f t_{sl}\left(\frac{\pi D^2}{4}\right)(1 - t_w f)\right] \quad (4)$$

The heat flux due to forced convection can be obtained according to the definition of local Stanton number St for turbulent convection is

$$Q_c = St\rho_l C_{pl} u_l (1 - A_q)(T_s - T_l) \quad (5)$$

where u_l is the adjacent liquid velocity.

The heat flux attributed to vapour generation is given by the energy carried away by the bubbles lifting off from the heated surface. It also represents the energy of vaporization whereby the bubble size of D_l is produced, which is expressed as

$$Q_e = R_f N_a f\left(\frac{\pi D_l^3}{6}\right)\rho_g h_{fg} \quad (6)$$

The total wall heat flux Q_w is the combination of the following heat flux components: $Q_w = Q_e + Q_{tc} + Q_{tcsl} + Q_c$. Note that for the case where there are no sliding bubbles, the wall heat partition model is similar to the Kurul and Podowski model.

2.2. Mechanistic approach for bubble frequency evaluation

The aforementioned improved wall heat partition model requires additional information: the bubble frequency (f).

As previously discussed, empirical correlations (such as Eq. (1)) are often adopted. In order to eliminate the uncertainty of applying empirical equations, the bubble frequency is proposed to be determined by a mechanistic approach based on the description of an ebullition cycle in nucleate boiling, which is formulated as

$$f = \frac{1}{t_g + t_w} \tag{7}$$

The waiting period (t_w) and the growth period of vapour bubbles (t_g) is derived from the transient conduction and force balance model, respectively. Details of the mechanistic approach are presented below.

2.2.1. Bubble waiting time (t_w)

When transient conduction occurs when a bubble slides or lifts off, the boundary layer gets disrupted and cold liquid comes in contact with the heated wall. Assuming that the heat capacity of the heater wall $\rho_s C_{ps} \delta_s$ is very small, the conduction process can be modelled by considering one-dimensional transient heat conduction into a semi-infinite medium with the liquid at a temperature T_l and the heater surface at a temperature T_s. The wall heat flux can be approximated by

$$Q_w = \frac{k_l (T_s - T_l)}{\delta_l} \tag{8}$$

where $\delta_l (= \sqrt{\pi \eta t})$ is the thickness of the thermal boundary layer. If the temperature profile inside this layer is taken to be linear (according to Hsu and Graham [17]), it can thus be expressed as

$$T_b = T_w - \frac{(T_s - T_l)x}{\delta_l} \tag{9}$$

where x is the normal distance from the wall. Based on the criterion of the incipience of boiling from a bubble site inside the thermal boundary layer, the bubble internal temperature for a nucleus site (cavity) with radius r_c is

$$T_b = T_{sat} - \frac{2\sigma T_{sat}}{C_2 r_c h_{fg} \rho_g} \quad \text{at} \quad x = C_1 r_c \tag{10}$$

where $C_1 = (1 + \cos\theta)/\sin\theta$ and $C_2 = 1/\sin\theta$. The angle θ represents the bubble contact angle. By substituting Eq. (10) into Eq. (9), the waiting time t_w can be obtained as

$$t = t_w = \frac{1}{\pi \eta} \left[\frac{(T_s - T_l) C_1 r_c}{(T_w - T_{sat}) - 2\sigma T_{sat}/C_2 \rho_g h_{fg} r_c} \right]^2 \tag{11}$$

The cavity radius r_c can be determined by applying Hsu's criteria and tangency condition of Eqs. (9) and (10), *viz.*,

$$t = \left[\frac{C_1 C_2 \rho_g h_{fg} r_c^2}{2\sigma T_{sat}} \right]^2 \frac{(T_s - T_l)^2}{\pi \eta} = \left[\frac{k_l}{Q_w} \right]^2 \frac{(T_s - T_l)^2}{\pi \eta} \tag{12}$$

From the above equation,

$$r_c = F \left[\frac{2\sigma T_{sat} k_l}{\rho_g h_{fg} Q_w} \right]^{1/2} \tag{13}$$

where,

$$F = \left(\frac{1}{C_1 C_2} \right)^{1/2} = \left(\frac{\sin^2 \theta}{1 + \cos\theta} \right)^{1/2}$$

According to Basu et al. [18], the factor F indicates the degree of flooding of the available cavity size and the wettability of the surface. If the contact angle $\theta \to 0$, all the cavities will be flooded. Alternatively, as $\theta \to 90°$, $F \to 1$, all the cavities will not be flooded (i.e. they contain traces of gas or vapour).

2.2.2. Force balance model and bubble growth time (t_g)

The development of the force balance model concentrates on the various forces that influence the growth of a bubble during flow conditions in the directions parallel and normal to a vertical heating surface. These forces are formulated according to the studies performed by Klausner et al. [1] and Zeng et al. [19]. Fig. 2 illustrates the forces acting on the bubble in the x-direction and y-direction; they are respectively,

$$\Sigma F_x = F_{sx} + F_{dux} + F_{sL} + F_h + F_{cp} \tag{14}$$

and

$$\Sigma F_y = F_{sy} + F_{duy} + F_{qs} + F_b \tag{15}$$

where F_s is the surface tension force, F_{du} is the unsteady-drag due to asymmetrical growth of the bubble and the dynamic effect of the unsteady liquid such as the history force and the added mass force, F_{sL} is the shear lift force, F_h is the force due to the hydrodynamic pressure, F_{cp} is the contact pressure force accounting for the bubble being in contact with a solid rather than being surrounded by liquid, F_{qs} is the quasi steady-drag in the flow direction, and F_b is the buoyancy force. In addition, g indicates the

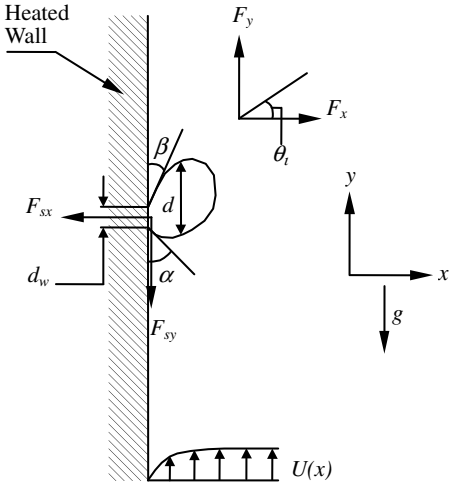

Fig. 2. Schematic drawings illustrating forces acting on a growing vapour bubble.

gravitational acceleration; α, β and θ_i are the advancing, receding and inclination angles, respectively; d_w is the surface/bubble contact diameter; and d is the vapour bubble diameter at the wall.

The forces acting in the x-direction can be estimated from

$$F_{sx} = -d_w\sigma\frac{\pi}{\alpha-\beta}[\cos\beta-\cos\alpha]; \quad F_{dux} = -F_{du}\cos\theta,$$
$$F_{sL} = \frac{1}{2}C_L\rho_l\Delta U^2\pi r^2; \quad F_h = \frac{9}{4}\rho_l\Delta U^2\frac{\pi d_w^2}{4},$$
$$F_{cp} = \frac{\pi d_w^2}{4}\frac{2\sigma}{r_r}$$

In the y-direction, they are

$$F_{sy} = -d_w\sigma\frac{\pi(\alpha-\beta)}{\pi^2-(\alpha-\beta)^2}[\sin\alpha+\sin\beta]; \quad F_{duy} = -F_{du}\sin\theta,$$
$$F_{qs} = 6C_D\mu_l\Delta U\pi r; \quad F_b = \frac{4}{3}\pi r^3(\rho_l-\rho_g)g$$

From the various forces described along the x-direction and y-direction, r is the bubble radius, ΔU is the relative velocity between the bubble centre of mass and liquid, C_D and C_L are the respective drag and shear lift coefficients and r_r is the curvature radius of the bubble at the reference point on the surface $x = 0$, which is $r_r \sim 5r$ (Klausner et al. [1]).

The drag coefficient C_D and shear lift coefficient C_L appearing in the drag and lift forces are determined according to the relationships proposed by Klausner et al. [1], *viz.*,

$$C_D = \frac{2}{3}+\left[\left(\frac{12}{Re}\right)^n+0.796\right]^{-1/n}$$
$$C_L = 3.877G_s^{-1/2}\left[\frac{1}{Re^2}+0.014G_s^2\right]^{1/4} \tag{16}$$

where $n = 0.65$ and $Re = \rho_l u_\tau x/\mu_l$ is the bubble Reynolds number. The dimensionless shear rate G_s is $(dU/dx)(r/\Delta U)$. The gradient dU/dx can be determined through the universal velocity profile for turbulent flow:

$$\frac{U}{u_\tau} = 2.5\ln(9.8x^+) \tag{17}$$

where u_τ is the friction velocity and $x^+ = \rho_l\Delta U d/\mu_l$ is the non-dimensional normal distance from the heated wall. The velocity profile in (17) is assumed to be applicable for the time-averaged velocity distribution in the vicinity of the heated wall. Adjacent velocities, determined through the two-fluid model, are used to obtain the varying local friction velocities through Eq. (17). These friction velocities are subsequently used to evaluate the gradients dU/dx along the heated wall to determine the shear rate G_s.

The growth force F_{du} is modeled by considering a hemispherical bubble expanding in an inviscid liquid, which is given by Zeng et al. [19] as

$$F_{du} = \rho_l\pi r^2\left(\frac{3}{2}C_s\dot{r}^2+r\ddot{r}\right) \tag{18}$$

where $\dot{}$ indicates differentiation with respect to time. The constant C_s is taken to be 20/3 according to Zeng et al. [19]. In estimating the growth force, additional information on the bubble growth rate is required. As in Zeng et al. [19], a diffusion controlled bubble growth solution by Zuber [20] is adopted:

$$r(t) = \frac{2b}{\sqrt{\pi}}Ja\sqrt{\eta t}; \quad Ja = \frac{\rho_l C_{pl}\Delta T_{sat}}{\rho_g h_{fg}}; \quad \eta = \frac{k_l}{\rho_l C_{pl}} \tag{19}$$

where Ja is the Jakob number, η is the liquid thermal diffusivity and b is an empirical constant that is intended to account for the asphericity of the bubble. For the range of heat fluxes investigated in this investigation, b is taken to be 0.21 based on a similar subcooled boiling study performed by Steiner et al. [21], which has been experimentally verified through their in-house measurements with water as the working fluid.

While a vapour bubble remains attached to the heated wall, the sum of the parallel and normal forces must satisfy the following conditions: $\Sigma F_x = 0$ and $\Sigma F_y = 0$. For a sliding bubble case, the former establishes the bubble departure diameter (D_d) while the latter yields the bubble lift-off diameter (D_l). The growth period t_g appearing in Eq. (7) can be readily evaluated based on the availability of the bubble size at departure from its nucleation site through Eq. (19). The lift-off period t_l can also be similarly calculated based on the bubble lift-off diameter. The difference between the bubble lift-off and bubble growth periods provides the period for the sliding bubble; the sliding distance l_s can subsequently be determined (see Fig. 1). An estimation on this sliding distance can be determined according to the experimental correlation of Maity [22] as $l_s = (2/3)C_v t_{sl}^{3/2}$ where t_{sl} is the sliding time $(t_l - t_g)$ and C_v is an acceleration coefficient correlated in terms of the tangential liquid velocity (u_l) adjacent to the heated surface: $C_v = 3.2u_l + 1$. This coefficient reflects the increase in bubble velocity with time after it begins to slide away from a nucleation site.

In reality, the surface/bubble contact diameter d_w evolves from the point of inception until the point of departure or lift-off. Here, a correlation based on the experimental data of Maity [22] as a function of the bubble contact angle θ is employed to determine the ratio of the bubble base diameter d_w to the bubble diameter at departure or lift-off, which is given as $C = 1 - \exp(-2\theta^{0.6})$. Experimental observations by Klausner et al. [1] and Bibeau and Salcudean [23] have indicated that the advancing angle α and receding angle β varied quite substantially during the sliding phase. Considering the complexity of the bubble departure and bubble lift-off, and the difficulty in obtaining the measurements, the advancing and receding angles can be reasonably evaluated through the bubble contact angle θ as $\alpha = \theta + \theta'$ and $\beta = \theta - \theta'$. Klausner et al. [1] have employed an angle θ' of 4.5° in their theoretical analysis while Bibeau and Salcudean [23] have reported a value of 2.5°. According to Winterton [24], the angle θ' has nonethe-

less been postulated to be as high as 10°. In the present study, an angle θ' of 5° is adopted. For the inclination angle θ_i, a value of 10° that gave the best fit to the data by Klausner et al. [1] is employed for the current force balance model. Based on the experimental observations of Zeitoun and Shoukri [13] and Lee et al. [15], the bubble contact angles have been taken to be at 35° and 45° for the present investigation.

2.3. Two-fluid model

The current numerical simulations are based on the two-fluid model approach. The Eulerian–Eulerian modelling framework is based on ensemble-averaged of mass, momentum and energy transport equations for each phase. Regarding the liquid phase (α_l) as continuum and the vapour phase (bubbles) as disperse phase (α_g), these equations can be written as Continuity equation of liquid phase

$$\frac{\partial \rho_l \alpha_l}{\partial t} + \nabla \cdot (\rho_l \alpha_l \vec{u}_l) = \Gamma_{lg} \tag{20}$$

Continuity equation of vapour phase

$$\frac{\partial \rho_g \alpha_g f_i}{\partial t} + \nabla \cdot (\rho_g \alpha_g \vec{u}_l) = S_i - f_i \Gamma_{lg} \tag{21}$$

Momentum equation of liquid phase

$$\begin{aligned}\frac{\partial \rho_l \alpha_l \vec{u}_l}{\partial t} + \nabla \cdot (\rho_l \alpha_l \vec{u}_l \vec{u}_l) = {} & -\alpha_l \nabla P + \alpha_l \rho_l \vec{g} \\ & + \nabla[\alpha_l \mu_i^e (\nabla \vec{u}_l + (\nabla \vec{u}_l)^T)] \\ & + (\Gamma_{lg} \vec{u}_g - \Gamma_{gl} \vec{u}_l) + F_{lg}\end{aligned} \tag{22}$$

Momentum equation of vapour phase

$$\begin{aligned}\frac{\partial \rho_g \alpha_g \vec{u}_g}{\partial t} + \nabla \cdot (\rho_g \alpha_g \vec{u}_g \vec{u}_g) = {} & -\alpha_g \nabla P + \alpha_g \rho_g \vec{g} \\ & + \nabla[\alpha_g \mu_g^e (\nabla \vec{u}_g + (\nabla \vec{u}_g)^T)] \\ & + (\Gamma_{gl} \vec{u}_l - \Gamma_{lg} \vec{u}_g) + F_{gl}\end{aligned} \tag{23}$$

Energy equation of liquid phase

$$\frac{\partial \rho_l \alpha_l H_l}{\partial t} + \nabla \cdot (\rho_l \alpha_l \vec{u}_l H_l) = \nabla[\alpha_l \lambda_l^e (\nabla T_l)] + (\Gamma_{gl} H_l - \Gamma_{lg} H_g) \tag{24}$$

Energy equation of vapour phase

$$\frac{\partial \rho_g \alpha_g H_g}{\partial t} + \nabla \cdot (\rho_g \alpha_g \vec{u}_g H_g) = \nabla[\alpha_g \lambda_g^e (\nabla T_g)] + (\Gamma_{gl} H_l - \Gamma_{lg} H_g) \tag{25}$$

The interfacial mass transfer rate due to condensation in the bulk subcooled liquid in Eq. (2) can be expressed by the following expression:

$$\Gamma_{lg} = \frac{h a_{if} (T_{sat} - T_l)}{h_{fg}} \tag{26}$$

Here, h indicates the inter-phase heat transfer coefficient which is correlated in terms of the Nusselt Number [4]. The wall vapour generation rate is modelled in a mechanistic manner by considering the total mass of bubbles detaching from the heated surface as

$$\Gamma_{gl} = \frac{Q_e}{h_{fg} + C_{pl}(T_{sat} - T_l)} \tag{27}$$

The total interfacial force F_{mn} appearing in Eq. (22) are formulated through appropriate consideration of different sub-forces affecting the interface between each phase. For the liquid phase, the interfacial forces F_{lg} are

$$F_{lg} = F_{lg}^{drag} + F_{lg}^{lift} + F_{lg}^{lubrication} + F_{lg}^{dispersion} \tag{28}$$

The terms appearing on the right hand side of Eq. (28) are drag force, lift force, wall lubrication force and turbulent dispersion force. More detail descriptions of these interfacial forces can be found in [25]. Note that for the gas phase, $F_{gl} = -F_{lg}$.

2.4. Population balance model

On the right hand side of Eq. (21), S_i represents the additional source terms due to coalescence and breakage for the range of bubble classes that can exist within the vapour phase. The MUlti-SIze-Group (MUSIG) population balance model originally developed by Lo [26] has been adopted to account for the non-uniform bubble size distribution in subcooled boiling flows. The model divides the continuous size range of bubbles into a number of discrete classes and assumes each bubble class travel at the same mean algebraic velocity. Continuity equation for the individual number density of bubble class i can be expressed as follow [27]:

$$\frac{\partial n_i}{\partial t} + \nabla \cdot (\vec{u}_g n_i) = \left(\sum_j R_j \right)_i + (R_{ph})_i \tag{29}$$

where $(\sum_j R_j)_i$ represents the net change in the number density distribution due to coalescence and break-up processes. The term $(R_{ph})_i$ constitutes the essential formulation of the source/sink rate for the phase change processes associated with subcooled boiling flow. Detailed expressions of these rates can be found in [11].

Here, the break-up rate of bubbles of volume v_j into volume v_i is modelled according to the model developed by Luo and Svendsen [28]. The model is developed based on the assumption of bubble binary break-up under isotropic turbulence situation. The daughter size distribution has been taken account using a stochastic breakage volume fraction f_{BV}. Incorporate the increase coefficient of surface area $c_f = [f_{BV}^{2/3} + (1 - f_{BV})^{2/3} - 1]$ into the breakage efficient, the break-up rate of bubbles can be obtained as

$$\frac{\Omega(v_j : v_i)}{(1-\alpha_g)n_j} = C\left(\frac{\varepsilon}{d_j^2}\right)^{1/3} \int_{\xi_{\min}}^{1} \frac{(1+\xi)^2}{\xi^{11/3}} \times \exp\left(-\frac{12 c_f \sigma}{\beta \rho_l \varepsilon^{2/3} d^{5/3} \xi^{11/3}}\right) d\xi \quad (30)$$

where $\xi = \lambda/d_j$ is the size ratio between an eddy and a particle in the inertial sub-range and consequently $\xi_{\min} = \lambda_{\min}/d_j$ and C and β are determined, respectively, from fundamental consideration of drops or bubbles breakage in turbulent dispersion systems to be 0.923 and 2.0.

On the other hand, bubble coalescence occurs via collision of two bubbles which may be caused by wake entrainment, random turbulence and buoyancy. However, only turbulence random collision is considered in the present study as all bubbles are assumed in spherical shape (wake entrainment becomes negligible). Furthermore, as all bubbles travel at the same velocity in the MUSIG model, buoyancy effect is also eliminated. The coalescence rate considering turbulent collision taken from Prince and Blanch [29] can be expressed as

$$\chi_{ij} = \frac{\pi}{4}[d_i + d_j]^2 (u_{ti}^2 + u_{tj}^2)^{0.5} \exp\left(-\frac{t_{ij}}{\tau_{ij}}\right) \quad (31)$$

where τ_{ij} is the contact time for two bubbles given by $(d_{ij}/2)^{2/3}/\varepsilon^{1/3}$ and t_{ij} is the time required for two bubbles to coalesce having diameter d_i and d_j estimated to be $[(d_{ij}/2)^3 \rho_l / 16\sigma]^{0.5} \ln(h_0/h_f)$. The equivalent diameter d_{ij} is calculated as suggested by Chesters and Hoffman [30]: $d_{ij} = (2/d_i + 2/d_j)^{-1}$. According to Prince and Blanch [29], for air–water systems, experiments have determined the initial film thickness h_0 and critical film thickness h_f at which rupture occurs to 1×10^{-4} and 1×10^{-8} m, respectively. The turbulent velocity u_t in the inertial sub-range of isotropic turbulence [31] is given by $u_t = \sqrt{2}\varepsilon^{1/3} d^{1/3}$.

3. Experimental details

For the axial measurements performed by Zeitoun and Shoukri [13], the test section was a vertical concentric annular test section. The inner tube, which had a 12.7 mm outside diameter, was a 30.6 cm long, thick-walled stainless-steel tube (0.25 mm thick) that was electrically heated. The entire inner tube was connected to a 55 kW DC power supply. The outer tube was a 25.4 mm inner diameter plexiglass tube that permitted visual observation. Distilled-degassed water was used as the working fluid. A digital image processing technique was used to analyze the high-speed video information and to measure bubble size distributions along the subcooled boiling region. A single beam gamma densitometer was used for the void fraction measurements.

For the local measurements performed by Yun et al. [14] and Lee et al. [15], the experimental setup consisted of a vertical concentric annulus with an inner heating rod of 19 mm outer diameter. The heated section was a 1.67 m long Inconel 625 tube with 1.5 mm wall thickness and filled with magnesium oxide powder insulation. The rod was uniformly heated by a 54 kW DC power supply. The outer wall comprised of two stainless-steel tubes with 37.5 mm inner diameter. The plane for measuring the radial distribution was located at 1.61 m downstream of the beginning of the heated section. Demineralised water was used as the working fluid. Local gas phase parameters such as local void fraction, bubble frequency and bubble velocity were measured by a two-conductivity probe method. The Sauter mean bubble diameters (assuming spherical bubbles) were determined through the IAC, calculated using the measured bubble velocity spectrum and bubble frequency. The uncertainties in the velocity measurements of the two axial and local experiments were within ±3.0%. Experimental conditions for the local and axial data that have been used for comparison with the simulated results are presented in Table 1.

Table 1
Experimental conditions for local (L1, L2, L3) and axial (A1, A2, A3) cases

Case	P_{inlet} (MPa)	T_{inlet} (°C)	T_{sub}(inlet) (°C)	Q_w (kW/m^2)	G (kg m^{-2} s^{-1})
A1	0.137	91.9	14.9	286.7	156.2
A2	0.150	94.6	16.6	508.0	264.3
A3	0.150	88.9	22.5	705.0	411.7
L1	0.143	96.9	13.4	152.9	474.0
L2	0.137	94.9	13.8	197.2	714.4
L3	0.143	92.1	17.9	251.5	1059.2

4. Numerical details

The conservation equations for mass, momentum and energy of each phase were discretised using the finite volume technique. A total number 15 bubble classes were prescribed for the dispersed phases, which are illustrated in Table 2 for the local and axial cases. This represents an additional set of 15 transport equations of which they were progressively solved and coupled with the flow equations during the simulations.

The advantage of an annular geometrical shape was utilized by modelling only one quarter of the annulus as the domain for both the local and axial cases since uniform wall heat flux was applied. A body-fitted conformal system was employed to generate the three-dimensional mesh within the annular channel resulting in a total of 13 (radial) × 30 (axial) × 3 (circumference) control volumes for the local case while a total of 8 (radial) × 20 (axial) × 3 (circumference) control volumes were used for the axial case. Since wall function was used in the present study to bridge the wall and the fully turbulent region away from heater surface, the normal distance between the wall and the first node in the bulk liquid should be such that the corresponding x^+ was greater than 30. Grid independence was examined. In the mean parameters considered, further grid

Table 2
Evaluated diameters of each discrete bubble classes for the local and axial cases

Bubble class	d_{local} (mm)	d_{axial} (mm)
1	0.45	0.29
2	0.94	0.61
3	1.47	0.95
4	2.02	1.31
5	2.58	1.67
6	3.14	2.03
7	3.71	2.40
8	4.27	2.76
9	4.83	3.13
10	5.40	3.49
11	5.96	3.86
12	6.53	4.23
13	7.10	4.59
14	7.66	4.96
15	8.23	5.32

refinement did not reveal significant changes to the two-phase flow parameters.

5. Result and discussion

The improved wall heat partition model is assessed against subcooled flow boiling of axial and local radial experimental data covering a wide range of different mass and heat fluxes.

5.1. Axial measurement by Zeitoun and Shoukri [13]

The predicted and measured profiles of the Sauter mean bubble diameter normalized by the length scale $\sqrt{\sigma/g(\rho_l-\rho_g)}$, void fraction and interfacial area concentration (IAC) ($a_{if}=6\alpha_g/D_s$) along the heated section are presented in Figs. 3–5. As depicted in Fig. 3, the predicted dimensionless Sauter mean bubble diameter profiles are seen to agree well against experimental data for all axial cases. It can be inferred that the bubble lift-off diameter and the following bubble coalescence/breakage are reasonably captured by the mechanistic force balance and population balance model. In general, the trends of sharp increasing void fraction along the heated section are in satisfactory agreement with measurements. However, void fractions near the channel exit were over-predicted in case A1 and were under-predicted in case A3. This could be attributed to the uncertainties embedded in estimating the active nucleation site density of the heated surface and the inter-phase heat transfer coefficient, which subsequently affect the calculated bubble generation and condensation rate. Without sufficient information, the active nucleation site and the inter-phase heat transfer coefficient have only been correlated as a function to the superheated temperature and to the Nusselt number. These correlations were however based on specific experimental data which may be inappropriate for Zeitoun and Shoukri's experiment. As the IAC is proportional to the void fraction and bubble diameter, the IAC profiles were also in satisfactory agreement with measurements.

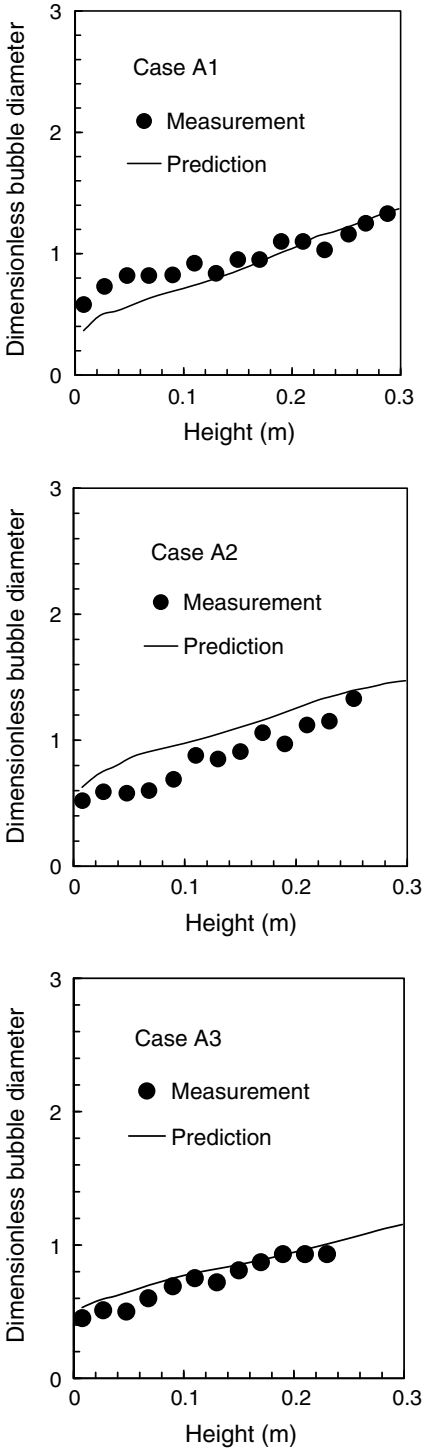

Fig. 3. Predicted axial dimensionless Sauter mean bubble diameter profiles and experimental data of Zeitoun and Shouskri [13].

Forces acting on the growing bubble for the bubble departure and lift-off diameters at the point before the channel exit are summarized in Table 3. Along the horizontal direction (perpendicular to the flow direction), the shear

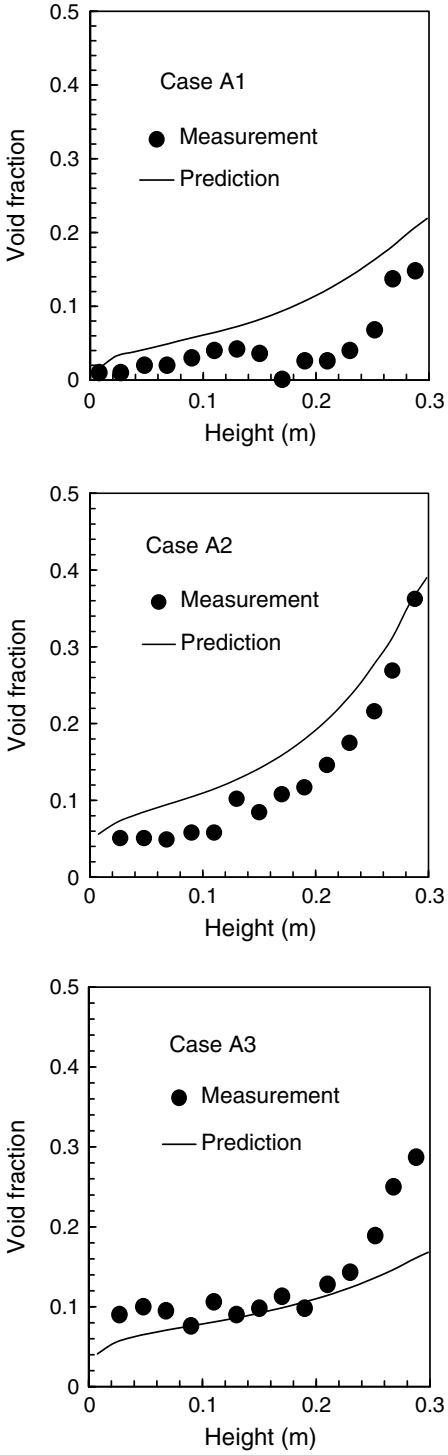

Fig. 4. Predicted axial void fraction profiles and experimental data of Zeitoun and Shouskri [13].

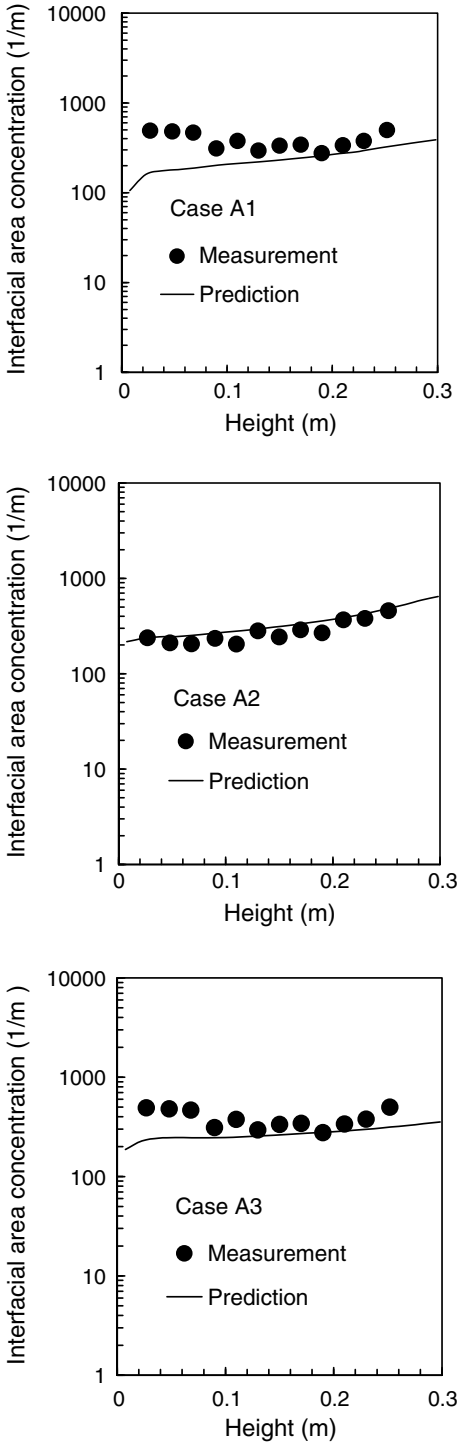

Fig. 5. Predicted axial interfacial area concentration profiles and experimental data of Zeitoun and Shouskri [13].

lift forces are seen to be the dominant forces overcoming the surface tension forces acting on the vapour bubbles. In the vertical direction, forces are dominated by the buoyancy forces thereby causing the vapour bubbles to first depart from the surface and later to slide along the heated surface. Based on the force balance model, the ratio of the predicted bubble lift-off diameter to the predicted bubble departure diameter ranged approximately between 2 and 3, which showed good agreement against experimental observations of Basu et al. [7].

The predicted wall heat flux partitions and its associated superheated and subcooling temperatures of adjacent liquid at the point of channel entrance and exit are tabulated in Table 4. Owing to the rather high heat fluxes,

Table 3
Predicted forces acting on growing vapour bubble and its associated bubble departure and lift-off (at the point of channel exit for axial cases; at the measuring station for local cases)

	Case A1	Case A2	Case A3	Case L1	Case L2	Case L3
Horizontal direction						
F_{sx} (N)	4.10×10^{-05}	4.10×10^{-05}	4.10×10^{-05}	5.06×10^{-05}	5.06×10^{-05}	5.06×10^{-05}
F_{dux} (N)	2.30×10^{-06}	3.10×10^{-06}	3.12×10^{-06}	1.46×10^{-06}	1.82×10^{-06}	1.90×10^{-06}
F_{sL} (N)	1.45×10^{-04}	1.50×10^{-04}	1.42×10^{-04}	1.78×10^{-04}	1.76×10^{-04}	1.71×10^{-04}
F_h (N)	3.50×10^{-06}	2.70×10^{-06}	4.10×10^{-06}	3.94×10^{-06}	4.09×10^{-06}	4.84×10^{-06}
F_{cp} (N)	3.36×10^{-06}	3.72×10^{-06}	4.24×10^{-06}	3.79×10^{-06}	4.25×10^{-06}	4.81×10^{-06}
D_l (mm)	1.65	1.48	1.31	1.45	1.31	1.20
Vertical direction						
F_{sy} (N)	7.26×10^{-07}	7.26×10^{-07}	7.22×10^{-07}	8.95×10^{-07}	8.95×10^{-07}	8.95×10^{-07}
F_{duy} (N)	3.58×10^{-07}	5.46×10^{-07}	5.51×10^{-07}	2.57×10^{-07}	3.21×10^{-07}	3.34×10^{-07}
F_{qs} (N)	1.28×10^{-06}	1.41×10^{-06}	1.48×10^{-06}	1.40×10^{-06}	1.46×10^{-06}	1.57×10^{-06}
F_b (N)	7.19×10^{-06}	1.04×10^{-05}	1.01×10^{-05}	6.96×10^{-06}	7.70×10^{-06}	7.39×10^{-06}
D_d (mm)	0.57	0.64	0.64	0.56	0.58	0.57

Table 4
Predicted heat partitions, superheat and subcooled temperatures of adjacent liquid at the point of channel entrance and (the channel exit for axial cases; the measuring station for local cases)

	Case A1	Case A2	Case A3	Case L1	Case L2	Case L3
Channel entrance						
Q_c	0%	0%	0%	100%	0%	100%
Q_{tc}	2.45%	2.78%	12.52%	0%	3.66%	0%
Q_{tcsl}	60.22%	46.83%	42.40%	0%	62.31%	0%
Q_e	37.33%	50.39%	45.08%	0%	34.03%	0%
T_{sup}	16.86	21.88	23.22	0.04	18.06	0.001
T_{sub}	14.56	15.20	19.05	11.30	11.24	13.57
Channel exit						
Q_c	0%	0%	0%	0%	0%	0%
Q_{tc}	1.69%	4.13%	18.60%	2.51%	4.56%	6.42%
Q_{tcsl}	46.68%	48.23%	44.83%	55.07	61.25%	65.58%
Q_e	51.63%	47.64%	36.57%	42.42%	34.19%	28.00%
T_{sup}	18.87	22.77	22.82	18.06	18.35	19.28
T_{sub}	4.31	2.33	6.62	4.06	4.49	8.38

vapour bubbles began to be generated right up the channel entrance and covered all the surface area along the heater. Heat flux partitions are primarily dominated by the surface quenching of sliding bubbles and the evaporation of the lift-off bubbles with the absence of heat flux partition due to single turbulence convection. It further confirms that transient conduction due to sliding bubbles is the dominant mode of heat transfer.

5.2. Local measurement by Yun et al. [14] and Lee et al. [15]

For the local cases of L1, L2 and L3, the measured and predicted radial profiles of the Sauter mean bubble diameter (D_s), vapour void fraction and interfacial area concentration located at the measuring plane 1.61 m downstream of the beginning of the heated section are shown in Figs. 6–8. Note that in all the figures, the dimensionless parameter $(r - R_i)/(R_o - R_i) = 1$ indicates the inner surface of the unheated flow channel wall while $(r - R_i)/(R_o - R_i) = 0$ indicates the surface of the heating rod in the channel.

As seen in Fig. 6, the predicted Sauter mean bubble diameter in the vicinity of the heated surface agreed well with measurement for all cases. It reflects that the bubble lift-off diameter is appropriately predicted by the force balance model. The presence of larger bubbles away from the heated wall confirms the occurrence of bubble coalescence. Further away from the heated wall, the reduction of the bubble sizes indicates the bubbles condensing due to the subcooled bulk liquid. In the vicinity of the outer wall (i.e. $(r - R_i)/(R_o - R_i) \geqslant 0.5$), bubble diameters are slightly over-predicted. Such errors may be caused by under-estimation of the subcooled condensation which is correlated to Nusselt number using empirical equation.

A closer examination of the local void fractions profile at the measuring station is presented in Fig. 7. Although the bubble lift-off diameter at the heater surface is appropriately estimated, void fraction near the heated surface is either over or under-predicted in cases L1 and L3, respectively. It reveals that the vapour generation rate due to evaporation is over or under-predicted. As previously indicated in the axial case, these errors could be caused by the inappropriate description of the active nucleation site den-

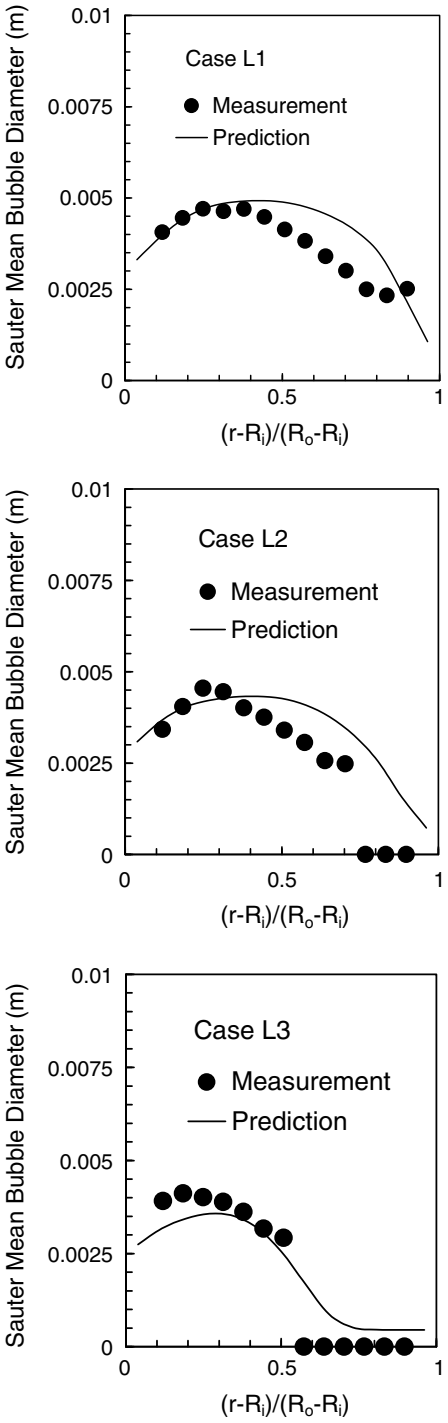

Fig. 6. Predicted local void fraction profiles and experimental data of Yun et al. [14] and Lee et al. [15] at the measuring plane.

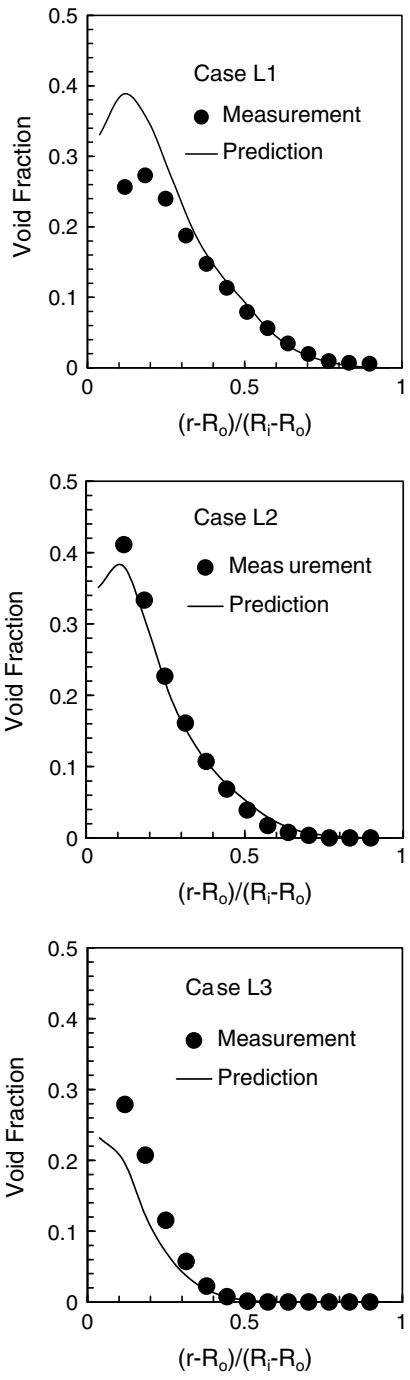

Fig. 7. Predicted local Sauter mean bubble diameter profiles and experimental data of Yun et al. [14] and Lee et al. [15] at the measuring plane.

sity correlation. The ICA profiles also showed similar trends with the void fraction distribution (see Fig. 8). Forces acting on the growing bubble as well as the bubble departure and lift-off diameters at measuring station are summarized in Table 3. Similar to the axial cases, the buoyancy forces and the shear lift forces are the dominating forces causing the bubble to depart and to lift-off from the heater.

The predicted wall heat flux partitions and its associated superheated and subcooling temperatures of adjacent liquid at the point of channel entrance and the measuring station are tabulated in Table 4. In cases L1 and L3, the superheated temperatures of the heater are appreciably small or close to zero at the point of channel entrance. Single-phase turbulence convection dominates within the subcooled boiling flow. Nevertheless, vigorous bubble generation has already

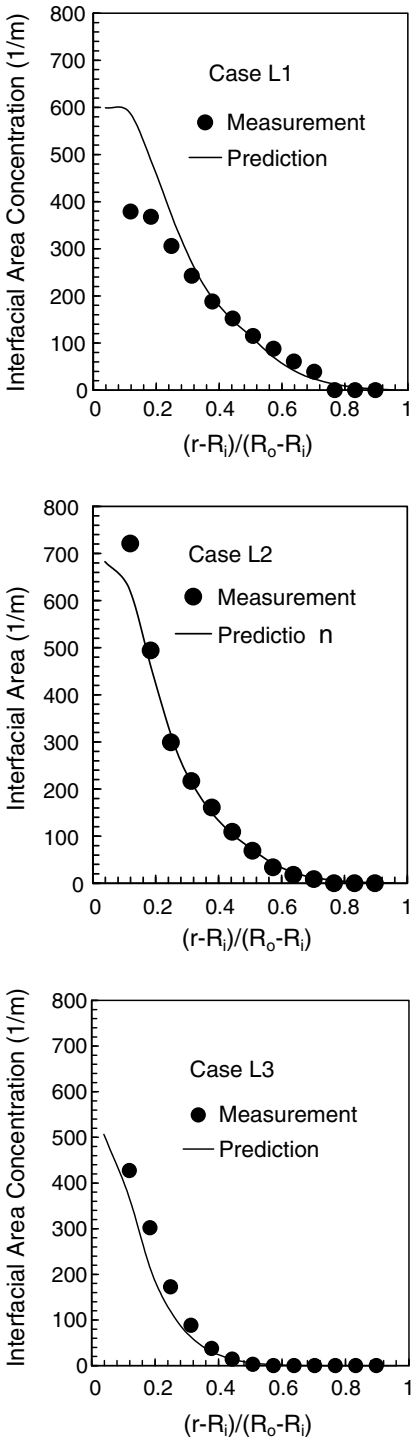

Fig. 8. Predicted local interfacial area concentration profiles and experimental data of Yun et al. [14] and Lee et al. [15] at the measuring plane.

emerged at the channel entrance at the same location of case L2 due to the higher heat flux being imposed. Based on the flow condition and forces acting on the bubbles, the evolution of heat flux partitions along the heater can be determined mechanistically. Owing to heat accumulation, surface quenching due to sliding bubbles and evaporation represent the dominant modes of heat transfer as exemplified at the measuring station near the channel exit.

6. Conclusions

Formulation of an improved wall heat flux partitioning model that accounted sliding bubbles alongside with the fundamental consideration of bubble frequency theory during low-pressure subcooled flow boiling has been presented. This model when coupled with a force balance model to predict forces acting on a vapour bubble growing under subcooled flow boiling demonstrated the capability to accommodate more complex analyses of bubble growth, bubble departure and bubble lift-off over a wide range of wall heat fluxes and flow conditions. The models were assessed against axial and local subcooled boiling flow measurements [13–15]. Comparison of the predicted results against local measurements showed good agreement for the profiles of Sauter mean bubble diameter, void fraction and interfacial area concentration.

Bubble departure and lift-off diameters that were determined mechanistically based on the force balance model showed good agreement against experimental observations of Basu et al. [7]. The predicted heat flux partitions ascertained that surface quenching due to sliding bubbles became the dominant mode of heat transfer. The influence of sliding bubbles is therefore significant and should be properly accounted. This present study successfully extended our previous model to account for the bubble sliding effect and incorporate with population balance model. Instead of applying empirical correlations, the current model mechanistically determines the complete ebullition description of the bubble growth, sliding, lift-off as well as the bubble coalescence and bubble breakage within the boiling flow system.

It should be noted that condensation heat transfer that may occur at the protruded tips of bubbles exposed to the bulk liquid has not been considered in the present model. As pointed out by Basu et al. [7], the effect of condensation may suppress the growth of bubble thereby causing the bubble to remain attached to the surface. In high subcooling flows, bubble lift-off diameter and its related evaporation heat transfer may be over-predicted by the present model. Accounting condensation heat transfer in future calculations features the next step of development of the mechanistic model.

Acknowledgment

The financial support provided by the Australian Research Council (ARC project ID DP0556095) is gratefully acknowledged.

References

[1] J.F. Klausner, R. Mei, D.M. Bernhard, L.Z. Zeng, Vapor bubble departure in forced convection boiling, Int. J. Heat Mass Transfer 36 (1993) 651–662.

[2] G.R. Warrier, V.K. Dhir, Heat transfer and wall heat flux partitioning during subcooled flow nucleate boiling – a review, ASME J. Heat Transfer 128 (2006) 1243–1256.

[3] N. Kurul, M.Z. Podowski, Multidimensional effects in forced convection subcooled boiling, in: Proceedings of the 6th International Heat Transfer Conference, Toronto, Hemisphere Publishing Corporation, Washington, 1978, pp. 115–120.
[4] J.Y. Tu, G.H. Yeoh, On numerical modelling of low-pressure subcooled boiling flows, Int. J. Heat Mass Transfer 45 (2002) 1197–1209.
[5] B. Končar, I. Kljenak, B. Mavko, Modeling of local two-phase parameters in upward subcooled flow boiling at low pressure, Int. J. Heat Mass Transfer 47 (2004) 1499–1513.
[6] R. Kumar, C.C. Maneri, T.D. Strayer, Modeling and numerical prediction of flow boiling in a thin geometry, ASME J. Heat Transfer 126 (2004) 23–33.
[7] N. Basu, G.R. Warrier, V.K. Dhir, Wall heat flux partitioning during subcooled flow boiling: Part I – model development, ASME J. Heat Transfer 127 (2005) 131–140.
[8] N. Basu, G.R. Warrier, V.K. Dhir, Wall heat flux partitioning during subcooled flow boiling: Part II – model validation, ASME J. Heat Transfer 127 (2005) 141–148.
[9] G. Sateesh, S.K. Das, A.R. Balakrishnan, Analysis of pool boiling heat transfer: effect of bubbles sliding on the heating surface, Int. J. Heat Mass Transfer 48 (2005) 1543–1553.
[10] R. Cole, A photographic study of pool boiling in the region of the critical heat flux, AIChE J. 6 (1960) 533–542.
[11] G.H. Yeoh, J.Y. Tu, Thermal-hydrodynamic modelling of bubbly flows with heat and mass transfer, AIChE J. 51 (2005) 8–27.
[12] G.H. Yeoh, J.Y. Tu, A unified model considering force balances for departing vapour bubbles and population balance in subcooled boiling, Nucl. Eng. Des. 235 (2005) 1251–1265.
[13] O. Zeitoun, M. Shoukri, Bubble behavior and mean diameter in subcooled flow boiling, ASME J. Heat Transfer 118 (1996) 110–116.
[14] B.J. Yun, G.-C. Park, C.H. Song, M.K. Chung, Measurements of local two-phase flow parameters in a boiling flow channel, in: Proceedings of the OECD/CSNI Specialist Meeting on Advanced Instrumentation and Measurement Techniques, 1997.
[15] T.H. Lee, G.-C. Park, D.J. Lee, Local flow characteristics of subcooled boiling flow of water in a vertical annulus, Int. J. Multiphase Flow 28 (2002) 1351–1368.
[16] R.L. Judd, K.S. Hwang, A comprehensive model for nucleate pool boiling heat transfer including microlayer evaporation, ASME J. Heat Transfer 98 (1976) 623–629.
[17] Y.Y. Hsu, R.W. Graham, Transport process in boiling and two-phase systems, Hemisphere, Washington, 1976.
[18] N. Basu, G.R. Warrier, V.K. Dhir, Onset of nucleate boiling and active nucleation site density during subcooled flow boiling, ASME J. Heat Transfer 124 (2002) 717–728.
[19] L.Z. Zeng, J.F. Klausner, D.M. Bernhard, R. Mei, A unified model for the prediction of bubble detachment diameters in boiling systems – II. Flow boiling, Int. J. Heat Mass Transfer 36 (1993) 2271–2279.
[20] N. Zuber, The dynamics of vapor bubbles in nonuniform temperature fields, Int. J. Heat Mass Transfer 2 (1961) 83–98.
[21] H. Steiner, A. Kobor, L. Gebhard, A wall heat transfer model for subcooled boiling flow, Int. J. Heat Mass Transfer 48 (2005) 4161–4173.
[22] S. Maity, Effect of velocity and gravity on bubble dynamics, MS Thesis, University of California, Los Angeles, 2000.
[23] E.L. Bibeau, M. Salcudean, A study of bubble ebullition in force convective subcooled nucleate boiling at low pressure, Int. J. Heat Mass Transfer 37 (1994) 2245–2259.
[24] R.H.S. Winterton, Flow boiling: prediction of bubble departure, Int. J. Heat Mass Transfer 27 (1984) 1422–1424.
[25] H. Anglart, O. Nylund, CFD application to prediction of void distribution in two-phase bubbly flows in rod bundles, Nucl. Sci. Eng. 163 (1996) 81–98.
[26] S. Lo, Application of population balance to cfd modelling of bubbly flow via the MUSIG model, AEA Technology, AEAT-1096, 1996.
[27] S. Kumar, D. Ramkrishna, On the solution of population balance equations by discretisation – I. A fixed pivot technique, Chem. Eng. Sci. 51 (1996) 1311–1332.
[28] H. Luo, H. Svendsen, Theoretical model for drop and bubble break-up in turbulent dispersions, AIChE J. 42 (1996) 1225–1233.
[29] M.J. Prince, H.W. Blanch, Bubble coalescence and break-up in air sparged bubble columns, AIChE J. 36 (1990) 1485–1499.
[30] A.K. Chesters, G. Hoffman, Bubble coalescence in pure liquids, Appl. Sci. Res. 38 (1982) 353–361.
[31] J.C. Rotta, Turbulente Stromungen, Teubner B.G., Stuttgart, 1972.